Discovering rare-earth-free magnetic materials through the development of a database

Masahiro Sakurai [1,*] Renhai Wang [2,3] Timothy Liao, [1,4] Chao Zhang [2] Huaijun Sun, [2] Yang Sun [2] Haidi Wang, [2,5]
Xin Zhao, [2] Songyou Wang, [6,7] Balamurugan Balasubramanian, [8] Xiaoshan Xu, [8] David J. Sellmyer, [8] Vladimir Antropov, [7]
Jianhua Zhang, [2] Cai-Zhuang Wang, [2,7,†] Kai-Ming Ho, [2,7] and James R. Chelikowsky [1,4,9]

[1]*Center for Computational Materials, Oden Institute for Computational Engineering and Sciences,*
The University of Texas at Austin, Austin, Texas 78712, USA
[2]*Department of Physics and Astronomy, Iowa State University, Ames, Iowa 50011, USA*
[3]*Department of Physics, University of Science and Technology of China, Hefei 230026, China*
[4]*Department of Physics, The University of Texas at Austin, Austin, Texas 78712, USA*
[5]*School of Electronic Science and Applied Physics, Hefei University of Technology, Hefei 230601, China*
[6]*Department of Optical Science and Engineering, Fudan University, Shanghai, 200433, China*
[7]*Ames Laboratory, U.S. Department of Energy, Ames, Iowa 50011, USA*
[8]*Nebraska Center for Materials and Nanoscience and Department of Physics and Astronomy, University of Nebraska,
Lincoln, Nebraska 68588, USA*
[9]*McKetta Department of Chemical Engineering, The University of Texas at Austin, Austin, Texas 78712, USA*

We develop an open-access database that provides a large array of datasets specialized for magnetic compounds as well as magnetic clusters. Our focus is on rare-earth-free magnets. Available datasets include (i) crystallography, (ii) thermodynamic properties, such as the formation energy, and (iii) magnetic properties that are essential for magnetic-material design. Our database features a large number of stable and metastable structures discovered through our adaptive genetic algorithm (AGA) searches. Many of these AGA structures have better magnetic properties when compared to those of the existing rare-earth-free magnets and the theoretical structures in other databases. Our database places particular emphasis on site-specific magnetic data, which are obtained by high-throughput first-principles calculations. Such site-resolved data are indispensable for machine-learning modeling. We illustrate how our data-intensive methods promote efficiency of the experimental discovery of new magnetic materials. Our database provides massive datasets that will facilitate an efficient computational screening, machine-learning-assisted design, and the experimental fabrication of new promising magnets.

I. INTRODUCTION

Magnets play an important role in a wide range of devices. They are key materials in modern technologies, such as cell phones, computers, electrical vehicles, wind turbines, and medical equipment. A major component of prototypical permanent magnets or magnetic recording materials is a $3d$ transition metal (typically iron), which provides a large amount of saturation magnetization. Most high-performance permanent magnets contain rare-earth elements, such as neodymium (Nd) and dysprosium (Dy). These "strategic" elements are of particular importance to improve performance in permanent-magnet applications [1–5].

The demand for rare-earth-based high-performance permanent magnets continues to grow, putting economical pressure on the supply of rare-earth elements. Concerns about the accessibility of rare-earth elements have stimulated theoretical and experimental efforts to improve the magnetic properties without relying on rare earths [6,7]. Similarly, permanent-magnet materials currently being used or considered as potential candidates for recording-media applications often contain expensive elements, such as Pt [8,9]. The search for new permanent-magnet materials free from critical rare earths and expensive metals is also important from the viewpoint of data-storage applications.

The design of a high-performance permanent magnet without rare-earth elements requires key magnetic properties to be optimized. These properties include (i) the saturation magnetic polarization J_s, (ii) the magnetic anisotropy energy (MAE) sufficient to induce high coercivity and a large maximum energy product, and (iii) the Curie temperature T_c. It is highly desirable to maximize these three quantities simultaneously for permanent-magnet applications. These key magnetic properties are macroscopic parameters that originate from the microscopic ("site-specific") magnetic properties, such as the local magnetic moments, the on-site spin-orbit anisotropy energies, and the pairwise magnetic exchange coupling parameters. Control of these site-specific magnetic properties is essential for optimizing the performance of permanent magnets.

*Present address: The Institute for Solid State Physics, The University of Tokyo, Kashiwa, Chiba 277-8581, Japan; sakurai@issp.u-tokyo.ac.jp
†wangcz@ameslab.gov

With advances in high-throughput first-principles calculations, there have been several efforts to combine first-principles calculations with data-science approaches, such as machine learning [10,11]. These efforts include the construction of an open-access database of materials, such as AFLOW [12,13], Materials Project [14,15], Open Quantum Materials Database [16,17], and the NOMAD repository [18]. Materials search can be accelerated by using extensive electronic-structure data, as demonstrated for new magnetic materials in Heusler alloys [19]. These databases cover a wide class of materials and provide basic material properties, such as elastic properties, thermodynamic properties, and band gap energies. However, none of them specifically focuses on magnetic materials. Several open databases [20–22] provide a small set of magnetic data for selected magnets. There remains a distinct lack of site-specific magnetic data, which are essential for the permanent-magnet design. In spite of its importance, the availability of dataset for magnetic clusters remains very sparse.

Here, we develop an open-access database of magnetic materials [23] to facilitate a data-intensive design of new rare-earth-free magnets. The remainder of the paper is organized as follows. In Sec. II, we present our theoretical framework to collect and generate a variety of materials data. In Sec. III, we give an overview of our database, along with statistics. In Sec. IV, we describe the details of available datasets, followed by notes about the unique features of our database in Sec. V. We illustrate in Sec. VI how our data-intensive methods promote efficiency of the experimental discovery of new magnetic materials. We give a perspective on the applications of our database in data science in Sec. VII and summarize this work in Sec. VIII.

II. METHODS FOR DATA GENERATION

A. Collection and generation of magnetic materials

We first collect Fe-based structures listed in the Materials Project database [15]. These include binary (Fe-X), ternary (Fe-X-X'), and quaternary (Fe-X-X'-X'') compounds, where X represents nonmagnetic (B, C, N, Al, Si, P, S, Ga, Ge, As, and Se) and magnetic (Ti, V, Cr, Mn, Co, Ni, Cu, Zn, Y, Zr, Nb, and Mo) species across the periodic table. Here, we select abundant nontoxic elements, such as B, C, and N, that can occupy interstitial sites when doped into Fe-based structures. Our selection also includes inexpensive metals, such as Ti and Zr, that can be alloyed with the main component of Fe. In a similar way, we collect Mn-based, Co-based, and Ni-based structures from the Materials Project.

We employ an adaptive genetic algorithm (AGA) [24,25] to discover new stable and metastable structures in a broader configuration space than contained within the Materials Project database. Our AGA search consists of a conventional genetic algorithm (GA) process and an "adaptive" process. In a conventional GA process, we use auxiliary classical potentials to optimize trial structures in a search pool. In an adaptive process, we update adaptively the auxiliary potential by matching it to density-functional theory (DFT) results on a subset of the optimized structures in the pool [26]. This strategy allows us to explore broad configuration space very

efficiently with keeping the accuracy of structure prediction. At every AGA step, trial structures are "filtered" in the spirit of Darwinian evolution. Structures with lower energies are reserved for the next step, whereas structures with higher energies are substituted by new ones that are generated from low-energy "parent structures." After dozens of AGA iterations, a search pool is populated by low-energy off-spring structures. For further details about AGA methods, see Refs. [7,27].

The formation energies of AGA-discovered structures are within a reasonable energy range above the convex hull, as shown for Zr-Co and Fe-Co-N systems [28,29]. Moreover, our AGA search is a useful method to identify new structures in experiment, as demonstrated for Co-N [30–32] and Li-Ni-B [33,34] systems. The latest version of our AGA code is implemented with an advanced search technique, which we call "symmetry-AGA," allowing us to narrow down search space and to discover new structures with a particular crystal symmetry.

B. First-principles calculations

We perform first-principles calculations to compute the thermodynamic and magnetic properties of crystalline magnetic materials collected from Materials Project and generated by the AGA. Our first-principles calculations are based on the DFT [35,36] combined with the projector-augmented wave (PAW) method [37]. We adopt a generalized gradient approximation (GGA) [38] for the exchange-correlation functional. We use a plane-wave basis set with a cutoff energy of 65 Ry to expand the valence wave functions. The Monkhorst-Pack scheme [39] is used to generate a k-point grid to perform Brillouin-zone integration. A k-point resolution of $2\pi \times 0.025$ Å^{-1} is used for spin-polarized calculations. All plane-wave calculations are carried out by using VASP [40,41] and QUANTUM ESPRESSO [42].

The MAE is defined as the total-energy difference between ferromagnetic states with different magnetization directions. The magnetic anisotropy energy, K, is written as

$$K^{a\text{-}c} = E_a - E_c. \tag{1}$$

Here, E_a (E_c) is the total energy for the magnetization oriented along the crystallographic a (c) axis. For uniaxial systems, positive $K^{a\text{-}c}$ value means that the c axis is the magnetization direction of the lowest energy, called the magnetic "easy axis." When $K^{a\text{-}c}$ is negative, the system has the easy axes in the ab plane. We incorporate the spin-orbit interactions in MAE calculations, where we use a finer mesh size of $2\pi \times 0.016$ Å^{-1} to achieve better convergence.

We adopt a static linear-response approach using Liechtenstein's formula [43] to compute the magnetic exchange coupling parameters, J_{ij}, in the long wavelength approximation. In this approach, we employ the linear muffin-tin orbital (LMTO) basis set [44] and the atomic sphere approximation (ASA) to Green's function method [45]. The momentum-space exchange coupling parameters, $J(q)$, are converted into the real-space ones, $J(r)$, by the fast Fourier transform technique. We use 41 points on an elliptical contour in the complex plane to carry out the energy integrals involved in the exchange parameter calculations. A k-point mesh with a resolution of $2\pi \times 0.025$ Å^{-1} has been used. We employed
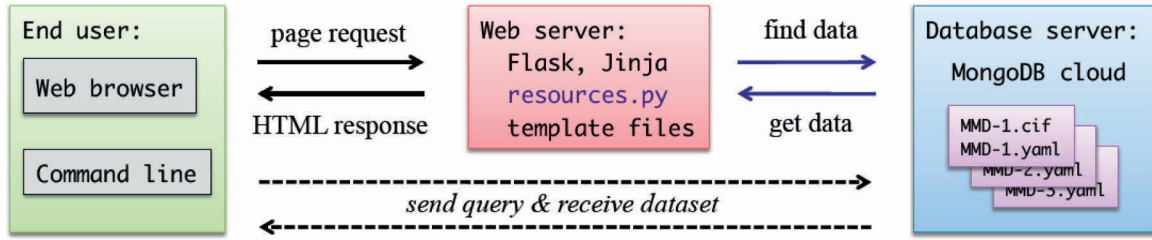
FIG. 1. A dataflow diagram of our Magnetic Materials Database [23].

the result of the classical Heisenberg model within the mean-field approximation to estimate the Curie temperature, T_c. We carefully tested this technique of the exchange coupling calculations for elemental ferromagnets, such as Fe, Co and Ni, in Ref. [46]. The electronic structure, T_c and J_{ij}, are calculated by using QUESTAAL [47].

C. Magnetic clusters

Magnetic clusters are constructed as fragments of bulk crystals, as has been done for Co_3N [48]. We also build icosahedral and cuboctahedral clusters for Fe, Co, and Ni [49–51], both of which have locally a closed-packed atomic coordination. Cluster geometry can be characterized by the atomic arrangement around the cluster core, the atomic coordination in a "mantle" region, and its surface structure (faceted or not). We carry out structural relaxations [52–54] for all magnetic clusters until a residual force is less than 0.01 Ry/a.u.

For magnetic clusters, we solve the Kohn-Sham equations on a uniform grid in *real space* as implemented in the PARSEC code [55–57]. The GGA-PBE functional is adopted for real-space DFT calculations. The Laplacian operator in the kinetic-energy term is expanded by using a high-order finite-differencing scheme. A grid spacing of 0.3 a.u. (approximately 0.16 Å) is sufficient to achieve the convergence of the total energy to within 1 meV/atom for $3d$ transition-metal systems [48–51,58]. We employ a spherical domain as a boundary condition to simulate an isolated cluster. The wave functions are sampled inside the domain and vanish beyond the domain boundary (typically 10 a.u. away from the outermost atom of a cluster). A notable feature of our real-space DFT code, PARSEC, is the use of a subspace filtering technique that exploits Chebyshev polynomials [59–61]. This filtering algorithm allows us to avoid explicit diagonalizations during the self-consistent field cycle.

III. DATABASE OVERVIEW

A. Data organization

Figure 1 illustrates the dataflow of our Magnetic Materials Database [23]. A data entry for an individual magnetic material is created with two file formats: (i) Crystallographic Information File (CIF) [62] and (ii) YAML (that stands for "YAML Ain't Markup Language" [63]). The CIF is a standard format in materials science to archive the crystallographic information. We use YAML, a popular data-serialization scheme, to store the computational results for the thermodynamic and magnetic properties. Two data files are processed with Python [64], an object-oriented programming language,

with the help of the Pymatgen libraries [65]. All the data are integrated into one location, building an online master database on the MongoDB cloud [66]. Upon finding new structures as well as finishing first-principles calculations, we append new data to the master database.

B. Database statistics

Table I summarizes the number of entries of our Magnetic Materials Database [23]. For crystal systems, a total of 3826 entries are registered at the time of this submission. These entries include the crystal structures taken from the Materials Project database [15] and those generated from our AGA techniques. By cross-checking all of the uploaded structures, we find a lesser degree of overlap between the two groups. This is because our AGA search yields not only stable compounds, but also many metastable structures, which are distributed in a wide range of chemical compositions. For magnetic clusters, our database contains a total of 1163 entries. Our magnetic clusters are elemental, binary, and ternary clusters, with sizes ranging from 5 to 22 Å in diameter. Our clusters have atomic sites of 9–490 with various Fe (Co) content.

Statistical data for crystal systems are given in Tables II and III. Our database contains magnetic materials for all seven crystal systems. Binary and ternary compounds account for 36% and 62% of the total number of entries, respectively. For binary (ternary) compounds, we have 114 (611) different combinations of two (three) elements. Each system is populated by dozens of structures with various chemical compositions (stoichiometry), with Fe-rich and Co-rich structures being in the majority.

Figures 2(a) and 2(b) compare the population of magnetic materials with respect to the stability (the formation energy above the convex hull) and the magnetic property (the saturation magnetic polarization), respectively.

TABLE I. The number of magnetic materials that are collected from the Materials Project (MP) database, discovered by our adaptive genetic algorithm (AGA), and from our cluster studies. The number in the parentheses denotes the overlap between the two groups.

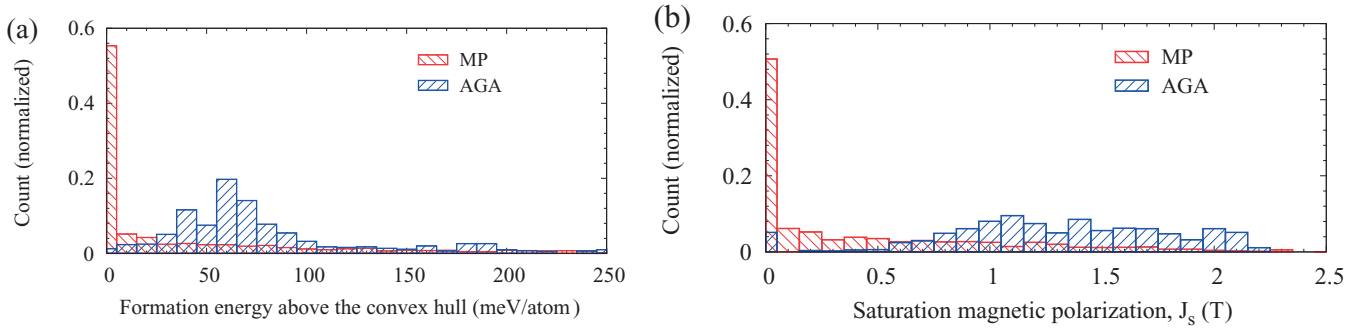| System | Crystal | | | |
	MP	AGA	(Overlap)	Cluster
Mn based	584	0	(0)	0
Fe based	787	290	(7)	929
Co based	714	594	(41)	151
Ni based	832	6	(0)	73

FIG. 2. Histogram charts that compare the population of two sets of magnetic materials with respect to (a) the formation energy above the convex hull and (b) the saturation magnetic polarization. The one group is from the Materials Project (MP) database, and the other group is from our adaptive genetic algorithm (AGA) searches.

Structures from Materials Project are very stable, with a sharp peak for the formation energies above the convex hull of 0–5 meV/atom. However, such stable structures have a very small magnetization value, as shown in Fig. 2(b). Most of our AGA structures have formation energies above the convex hull of less than 200 meV/atom, with a broad peak centered around 60 meV/atom. AGA structures in such an energy range can be accessible in experiment, as we will illustrate in Sec. VI. It is evident in Fig. 2(b) that our AGA structures have larger magnetization values than Materials Project structures.

C. Data availability

We provide end users with our data through our portal web page [23]. Our web server applications are developed with the Flask framework [67] powered with the Jinja template engine [68], as shown in the middle of Fig. 1. Our web applications are deployed on Heroku [69], a cloud-based application platform, where we use (i) Python scripts to load datasets from the master database, (ii) numerical libraries to carry out mathematical operations, and (iii) the Matplotlib utilities [70] to visualize data. This framework makes it possible to serve an automated, dynamic web page as well as to draw diagrams on demand. All the diagrams generated on our web applications are available in the Portable Network Graphics (png) format. Page viewers can download individual images.

IV. DESCRIPTION OF DATASET

In this section, we describe dataset details for Magnetic Materials Database [23]. Available data include crystallo-

graphic data, the thermodynamic properties, macroscopic and microscopic ("site-specific") magnetic properties, computational details, and references. Our database contains these data for crystalline phases and nanoclusters.

A. Crystallography

Our database provides crystallographic data for all entries. Available crystallographic dataset includes crystal system, space group (the Hermann-Mauguin notation and the international number [71]), chemical composition in a reduced formula, unit cell volume, lattice parameters, and atomic positions (Wyckoff positions and fractional coordinates). Table IV lists an example dataset of an Fe_5CoN_2 compound, which is discovered through our AGA search. We assign an entry ID of MMD-17 to this compound. On our database, the lattice parameters and atomic positions are available in various file formats: CIF, POSCAR (an input file format for VASP), an input file format for LAMMPS (a classical molecular dynamics code [72]), JSON (JavaScript Object Notation) [73], and YAML.

B. Thermodynamic properties

The thermodynamic properties, such as the formation energy, are tabulated and visualized on the web page for an individual structure. Based on DFT calculations, the formation energies are calculated with respect to a linear combination of the total energies of reference elemental phases.

As an example, we show in Fig. 3 the compositional phase diagram of an Fe-Si system, where the calculated formation energies are plotted as a function of the atomic fraction of Fe. In Fig. 3, a set of lines connecting the stable phases forms a

TABLE II. The number of entries and its percentage to the total for seven crystal systems.

Crystal system	Entries	Percentage
Triclinic	243	6%
Monoclinic	526	14%
Orthorhombic	934	24%
Tetragonal	594	16%
Trigonal	342	9%
Hexagonal	421	11%
Cubic	766	20%

TABLE III. The number of entries and the number of combination of three elements for elemental system, binary, ternary, and quaternary compounds.

System	Entries	Combinations
Elemental	59	15
Binary	1372	114
Ternary	2349	611
Quaternary	46	35

TABLE IV. The crystallographic data of Fe_5CoN_2.

Key	Value		
Entry ID	MMD-17		
Crystal system	orthorhombic		
Space group	$Amm2$ (No. 38)		
Chemical formula	Fe_5CoN_2		
Formula unit(s)	2		
Lattice parameters	$a = 3.834$, $b = 3.764$, $c = 11.162$ Å		
	$\alpha = 90.0$, $\beta = 90.0$, $\gamma = 90.0$ (deg.)		
Volume	161.063 Å^3		
Density	7.550 g/cm^3		
Atomic positions[a]	Fe	2a	(0.00000, 0.00000, 0.18331)
	Fe	2a	(0.00000, 0.00000, 0.49958)
	Fe	2b	(0.50000, 0.00000, 0.34649)
	Fe	2b	(0.50000, 0.00000, 0.67654)
	Fe	2b	(0.50000, 0.00000, 0.99567)
	Co	2a	(0.00000, 0.00000, 0.83344)
	N	2a	(0.00000, 0.00000, 0.00000)
	N	2b	(0.50000, 0.00000, 0.17748)
Source	AGA search		

[a]Element symbol, Wyckoff position, and fractional coordinates.

convex hull, which represents a plausible lower limit in the formation energy of this system. It is evident that the great majority of our AGA structures are distributed in the vicinity of the convex hull (within ~50 meV/atom above the hull) over a wide range of the Fe concentration. Such low-energy metastable structures are possible candidate phases, which can be reached out by using advanced fabrication techniques as we will illustrate in Sec. VI.

A compositional phase diagram of a ternary system can be shown as a projection of a three-dimensional energy curve onto two dimensions. Figure 4(a) shows the triangular phase diagram of an Fe-Co-N system. A two-dimensional projection of the minimum-energy surface, indicated by the black solid
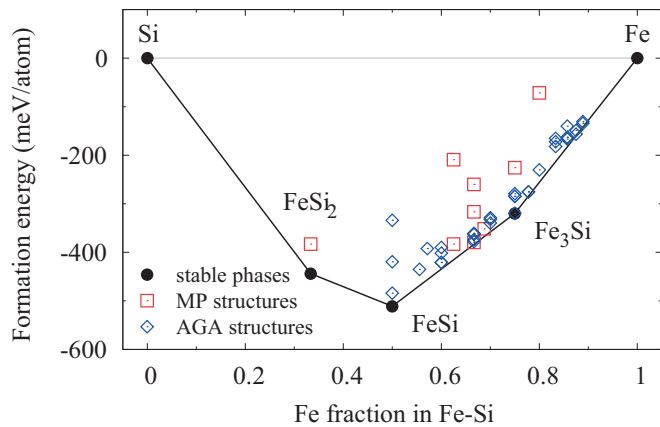

FIG. 3. Phase diagram of a binary Fe-Si system. The formation energies are plotted as a function of the Fe content. Crystal structures are taken from Materials Project (MP) and discovered through our adaptive genetic algorithm (AGA). A set of the solid lines that connect stable phases, called the convex hull, represents the theoretical lower limit in this compositional phase diagram. The closer it is to the convex hull, the more likely it is for the material to exist.

TABLE V. Example dataset for the thermodynamic and magnetic properties of Fe_5CoN_2 (MMD-17).

Key	Value
Thermodynamic properties	
Formation energy (vs elemental phases)	-14.7 meV/atom
Formation energy above convex hull	$+77.1$ meV/atom
Magnetic properties	
Total magnetic moment	23.88 μ_B/cell
Magnetic saturation polarization J_s	1.73 T
Magnetic easy axis	c
Magnetic anisotropy constant $K^{a\text{-}c}$	1.47 MJ/m^3
Magnetic anisotropy constant $K^{b\text{-}c}$	2.56 MJ/m^3
Magnetic anisotropy constant $K^{b\text{-}a}$	1.09 MJ/m^3
Magnetic hardness parameter κ[a]	0.79
Curie temperature T_c	1534 K

[a]See text for definition.

lines in Fig. 4(a), divides the compositional space into the Gibbs triangles. The formation energies above the convex hull of the structures from Materials Project (13 entries) are in the range of 0.1–0.4 eV/atom, whereas those of our AGA-discovered Fe- and Co-rich structures (258 out of 259 entries) are less than 0.1 eV/atom. The MMD-17 Fe_5CoN_2 phase is among such AGA structures, and its formation energy is listed in Table V.

In addition to a ternary phase diagram of the formation energy, we provide a ternary contour map of the magnetic saturation polarization as shown in Fig. 4(b). Contour lines and color gradation aid in the analysis of the landscape of the magnetic saturation polarization in a ternary system, along with the stability.

C. Macroscopic magnetic properties

Our database focuses on three macroscopic magnetic properties as key parameters for permanent-magnet design: (i) the magnetic saturation polarization J_s, in units of Tesla, (ii) the magnetic anisotropy constant K, in units of MJ/m^3, and (iii) the Curie temperature T_c, in units of Kelvin. The magnetic saturation polarization is related to the saturation magnetization M_s, through $J_s = \mu_0 M_s$, with μ_0 being the permeability of free space. These magnetic properties, along with related magnetic properties, are tabulated on an individual web page. An example dataset is given in Table V.

The magnetic saturation polarization and the total magnetic moment (Bohr magneton, μ_B, per unit cell, neglecting the orbital magnetic moments) are available for all structures. For structures with large magnetization ($J_s \geqslant 1$ T), we determine the magnetic anisotropy constant $K^{a\text{-}c}$ and the magnetic easy axis. In particular, our database provides multiple K values ($K^{a\text{-}c}$, $K^{b\text{-}c}$, and $K^{b\text{-}a}$) for orthorhombic, monoclinic, and triclinic crystal systems, as listed in Table V for the orthorhombic Fe_5CoN_2 phase (MMD-17). Our magnetic dataset also includes a dimensionless parameter,

$$\kappa = \sqrt{|K|/(\mu_0 M_s^2)}, \qquad (2)$$

called the "magnetic hardness parameter." The parameter κ has been recognized as a useful measure to assess the potential
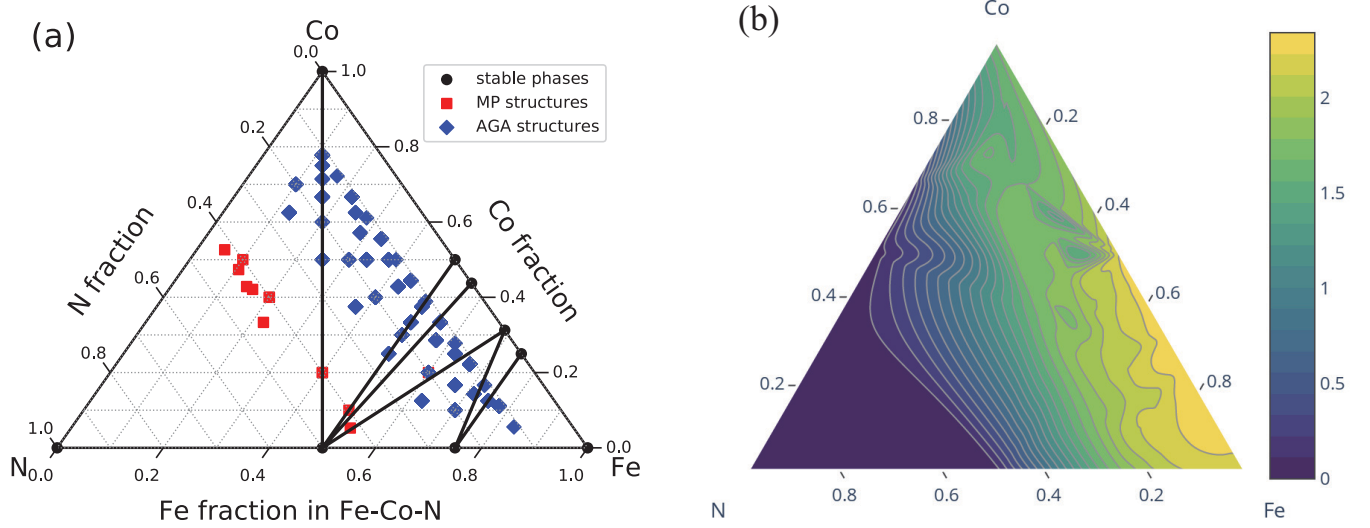
FIG. 4. (a) Compositional phase diagram of a ternary Fe-Co-N system. Crystal structures are taken from Materials Project (MP) and discovered through our adaptive genetic algorithm (AGA). The solid lines indicate the convex hull, a two-dimensional projection of the minimum-energy surface. (b) A contour plot of the magnetic saturation polarization in an Fe-Co-N system.

of magnetic materials for use as a permanent magnet [3,74]. The Curie temperature T_c is estimated for structures with $J_s \geqslant$ 1 T and $K \geqslant 1$ MJ/m^3.

Figures 5(a) shows the comparison of the theoretical and experimental values of the saturation magnetic polarization J_s. The calculated J_s values agree well with the experimental values in a wide range of J_s. In particular, there is an excellent agreement for materials with $J_s > 1$ T, making it possible to capture the J_s behavior of Fe-based and Co-based systems on an equal footing.

In Fig. 5(b), we plot our theoretical values of the magnetic anisotropy constant K for several existing rare-earth-free magnets. Overall, there is a good agreement between theory and experiment. We find a significant underestimation of K by about a factor of 2 for some exceptional systems with a large K, such as YCo$_5$. Still, our DFT results agree with the earlier work that reports a similar level of underestimation by the DFT framework [75].

Figure 5(c) shows the Curie temperature T_c, calculated for prototypical magnets. A percentage error between experimental values and our theoretical values is less than 20% for most of systems. We confirm that our LMTO-ASA approach combined with the mean-field approximation works well for estimating the T_c for various kinds of Fe-based and Co-based alloys.

D. Site-specific magnetic properties

Our database places a strong emphasis on the site-specific magnetic properties: (i) the local magnetic moments, (ii) the site-resolved spin-orbit coupling anisotropy energies, and (iii) the pairwise magnetic exchange coupling parameters. These microscopic quantities are key parameters for controlling the macroscopic magnetic properties, as well as for building machine-learning models for permanent-magnet design.
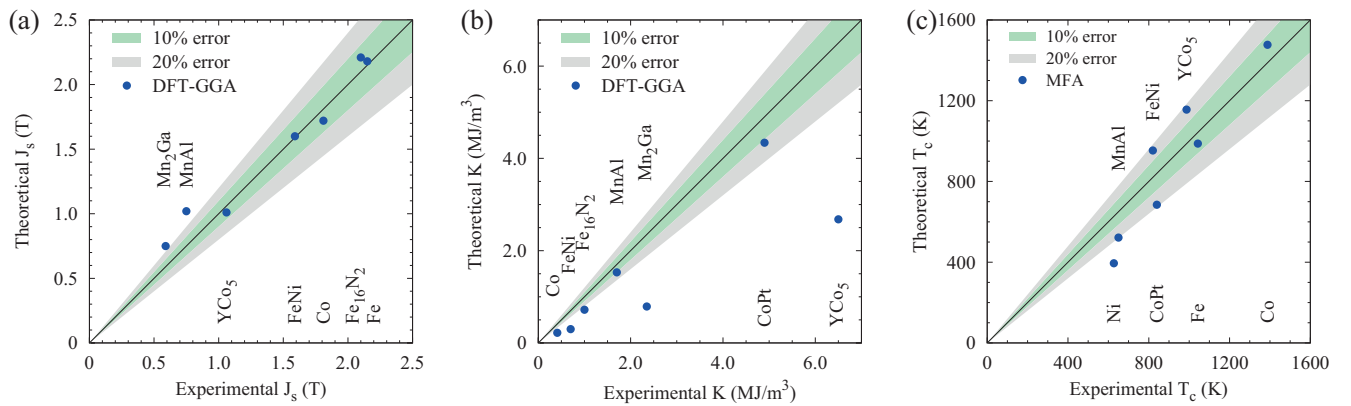

FIG. 5. Comparison of the theoretical and experimental values of (a) the saturation magnetic polarization J_s, (b) the magnetic anisotropy constant K, and (c) the Curie temperature T_c. We carry out DFT-GGA calculations for computing J_s and K, whereas we adopt the mean-field approximation (MFA) to estimate T_c. The reference materials are given in each plot. The shaded areas indicate the relative errors to the experimental values.
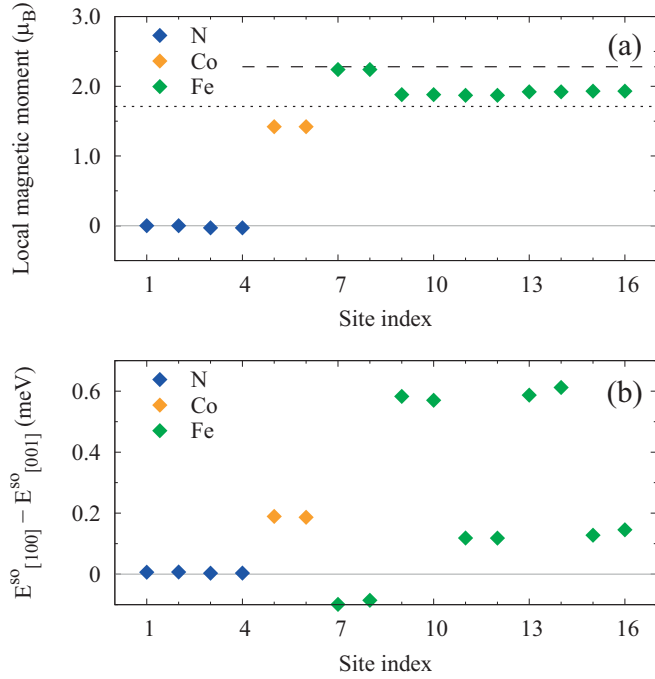
FIG. 6. Examples of the site-specific magnetic properties available on our Magnetic Materials Database [23]. (a) The local magnetic moments, m_i in units of μ_B/atom, of an atomic site i for Fe_5CoN_2 [an entry ID of MMD-17 (Table IV)]. The dashed and dotted lines indicate the values in bcc Fe and hcp Co, respectively. (b) The site-resolved spin-orbit coupling anisotropy energies of Fe_5CoN_2 (MMD-17) for the spin moments along the [100] and [001] directions.

Figure 6(a) shows the local magnetic moments of the Fe_5CoN_2 phase tagged with MMD-17 (Table IV). The local magnetic moment at site i is defined as

$$m_i = \int_{\Omega_i} \left[\rho_\uparrow(\vec{r}) - \rho_\downarrow(\vec{r}) \right] d^3 r. \tag{3}$$

Here, $\rho_{\uparrow(\downarrow)}$ denotes the electron density of the majority (minority) spin and Ω_i is a spherical domain centered on site i.

Figure 6(b) shows the site-resolved spin-orbit coupling anisotropy energies of the Fe_5CoN_2. The atomic spin-orbit coupling anisotropy energy at site i can be defined as

$$E_{a-c}^{SO}(i) = E_a^{SO}(i) - E_c^{SO}(i). \tag{4}$$

Here, $E_a^{SO}(i)$ and $E_c^{SO}(i)$ are the local spin-orbit coupling energies at site i with the spin moments aligned to the a and c axis, respectively. It has been shown [76] that this difference is directly related to the total magnetic anisotropy being twice larger in general:

$$K^{a-c} = \frac{1}{2} \sum_i E_{a-c}^{SO}(i). \tag{5}$$

It is evident that these microscopic magnetic parameters vary from site to site. The site-resolved magnetic data is indispensable for the detailed analysis of the macroscopic magnetic properties as well as data-intensive design of new permanent magnets.
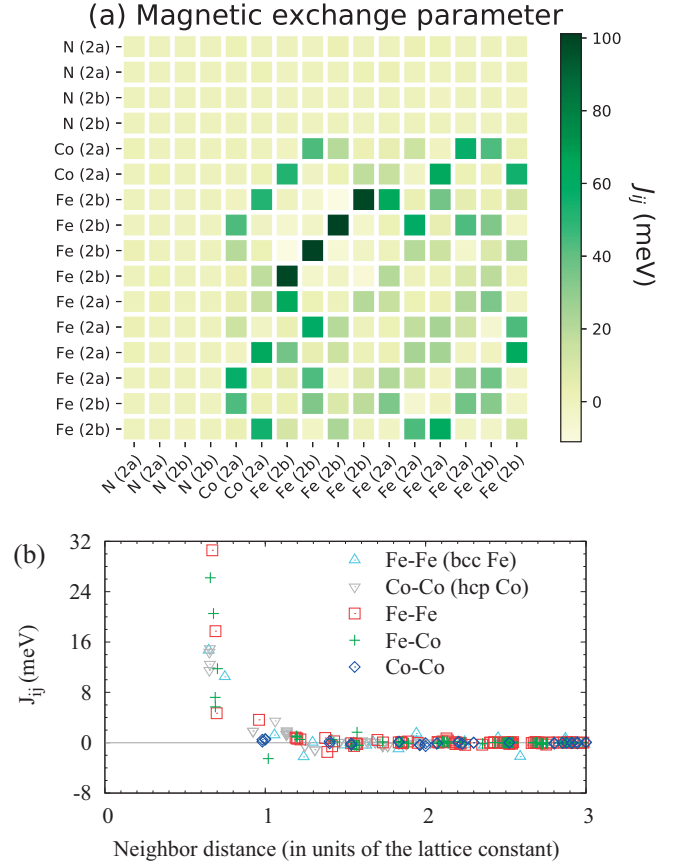

FIG. 7. Examples of pairwise magnetic properties available on our Magnetic Materials Database [23]. (a) The magnetic exchange coupling parameters J_{ij}, between two atomic sites in Fe_5CoN_2 (MMD-17). (b) Individual J_{ij} values as a function of the neighbor distance scaled with the lattice constant of Fe_5CoN_2 ($a = 3.834$ Å). The J_{ij} values in bcc Fe and hcp Co are also shown for comparison.

In Fig. 7(a), we visualize the pair-resolved magnetic exchange coupling parameters J_{ij} in a two-dimensional heat map. The magnitude of the exchange coupling between site i and j is shown on each colored cell. We take the Fe_5CoN_2 phase (entry ID of MMD-17) as an example. The plot is helpful to understand which pair is responsible for a large magnetic coupling.

Figure 7(b) shows the spatial dependence of J_{ij} in Fe_5CoN_2 (MMD-17). We plot the J_{ij} values in bcc Fe and hcp Co for comparison. It is evident that magnetic interactions between different types of atomic sites have different spatial behavior. Large magnetic couplings occur between Fe-Fe and Fe-Co pairs in Fe_5CoN_2, whereas the Co-Co couplings of this system are highly suppressed in comparison to those in hcp Co. The coupling parameters practically vanish when the neighbor distance goes beyond two lattice constants (~8 Å).

E. Cluster data

In addition to datasets for crystalline systems, our database provides a large amount of data for magnetic nanoclusters. In spite of their importance, cluster data is extremely sparse as most of the open-access databases focus only on crystalline
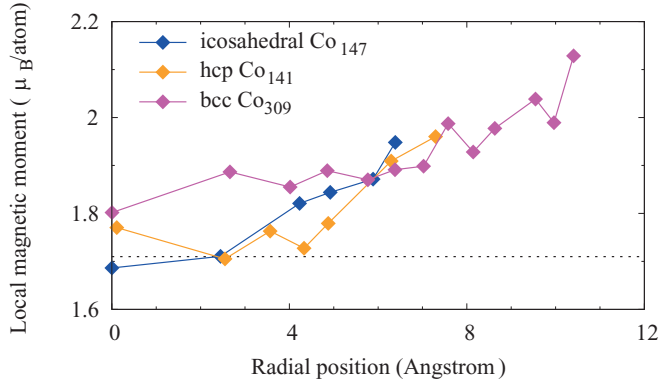
FIG. 8. Evolution of the local magnetic moments in Co clusters with different sizes and local atomic coordinations. The dotted line indicates the value of Co bulk (hcp).
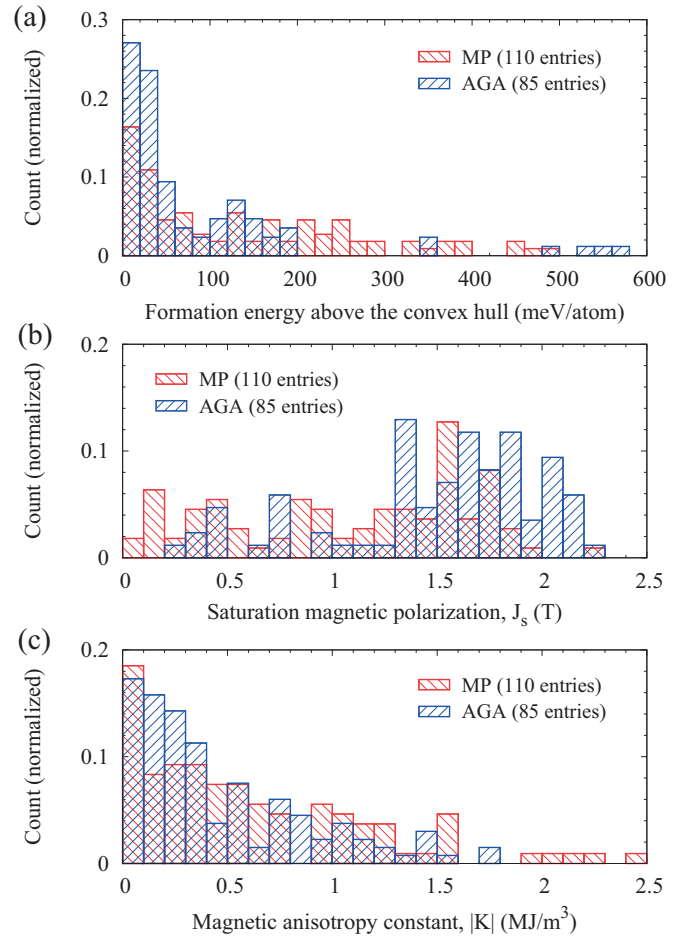

FIG. 9. Histogram charts that compare the population of Fe-based binary structures with respect to (a) the formation energy above the convex hull, (b) the saturation magnetic polarization, and (c) the magnetic anisotropy constant (absolute value). Two sets of structures are from either Materials Project (MP) or our adaptive genetic algorithm (AGA).

magnetic materials. Our datasets include (i) structural information, such as chemical species and their atomic position in the Cartesian coordinates, (ii) stability, such as the binding energy, and (iii) the magnetic properties, such as the total and local magnetic moments. For magnetic clusters, a total of 1153 entries have been registered so far (Table I).

Figure 8 shows the spatial variation of the local magnetic moments in Co clusters with three different atomic coordinations [hcp, bcc, and iscosahedral (fcc-like)]. Overall, the local magnetic moments grow steadily as going from the interior toward the surface. The local magnetic moments in a core region are a bulklike value ($\sim 1.7\ \mu_B$), whereas those near the surface are greatly enhanced because surface atom has fewer neighbors, resulting in stronger spin polarization [49–51].

F. Computational details and references

In addition to the structural and magnetic properties, the computational details and references are given on our database web pages. Computational details include notes about the methodology and numerical parameters, such as convergence criteria and *k*-point grids. Reference entries are original research papers and/or a uniform resource locator (URL) link to external databases.

V. UNIQUE FEATURES

A. Friendliness to data science

Our magnetic materials database is specifically designed for the state-of-the-art applications in data science and informatics, such as machine-learning algorithms. A whole set of the above-mentioned data is stored in an online storage at the MongoDB database cloud [66], where all the data items are indexed in a "machine-readable" format (Python Dictionary). The datasets of our database are open to the public through our portal web page [23]. As illustrated in Fig. 1, end users can communicate directly to our online database. End users can request a dataset by sending a query string to the database server using the standard MongoDB scheme. Upon user request, the database server will make a response to return a dataset in a user-friendly format, being suitable for building (or "training") a machine-learning model.

Our database server is implemented with data-filtering methods so that the server can handle various search keys: element(s), chemical formula, space group number, and the magnetic easy axis. With these search filters, end users can narrow down search results and look up specific structures very easily.

B. Promising novel structures from AGA searches

Our database provides many rare-earth-free structures that are discovered through AGA searches. We note that some of our AGA structures have better magnetic properties *and* are lower in the formation energy (namely, more stable) than the structures on other open databases. In Figs. 9(a)–9(c), we compare the population of Fe-based structures with respect to the stability and magnetic properties. Here, we prepare two sets of binary Fe-*X* structures (with *X* being B, C, N, Si, P, S, and Ge): one from our AGA search (85 entries) and another from Materials Project (110 entries). The majority of the AGA structures have the formation energies above the convex hull of less than 200 meV/atom. In particular, the AGA group has
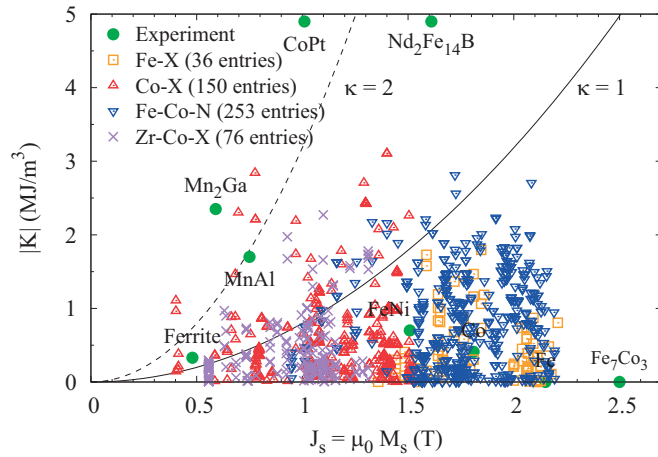
FIG. 10. The magnetic anisotropy constant in its absolute value $|K|$ versus the saturation magnetic polarization J_s for known magnets and AGA-discovered rare-earth-free magnets. The parabolic curves indicate the magnetic hardness parameter, $\kappa = \sqrt{|K|/(\mu_0 M_s^2)}$, of 1 (solid) and 2 (dashed).

a high population below 60 meV/atom. In contrast, the MP structures are widely distributed. Figure 9(b) shows that the AGA group is populated with structures with a larger saturation magnetic polarization ($1.3 \leqslant J_s \leqslant 2.2$ T) in comparison to the MP group. As shown in Fig. 9(c), the two groups are similar in distribution regarding the magnetic anisotropy constant. These analyses mean that the AGA structures are advantageous to exhibit a higher maximum energy product.

We illustrate another strong point of our AGA methodology in Fig. 10, where we plot K versus J_s for AGA structures enriched with Fe and/or Co. We also plot the experimental data of popular magnets for comparison. In terms of the saturation magnetic polarization, the Fe-based and FeCo-based AGA structures are distributed mostly in the range of 1.5–2.2 T, whereas the Co-based and ZrCo-based AGA structures are distributed in a region between 0.5 and 1.5 T. In terms of the magnetic anisotropy, one third of the AGA structures exhibit a decent magnitude of K ($\geqslant 1$ MJ/m^3) without relying on the critical elements. Moreover, about 10% of the AGA structures are identified as "hard" magnetic phases. Their magnetic hardness parameters κ are greater than 1.0, a recommended value for the use as permanent magnets. In fact, Nd$_2$Fe$_{14}$B, the strongest permanent magnet to date, takes a κ value of 1.54. Several AGA structures of Fe-Co-N, Co-X (X = N, Si, Ge), and Zr-Co-X (X = B, C, N) are predicted to have a decent κ value comparable to that of Nd$_2$Fe$_{14}$B. These AGA structures are promising candidate phases that yield a sufficient maximum energy product.

VI. GUIDANCE FOR EXPERIMENTAL DISCOVERY

Our AGA searches and advanced electronic-structure calculations guide efficiently the discovery of new magnetic materials, where experimentalists use nonequilibrium fabrication methods, such as high-pressure sputtering (or cluster deposition) and rapid quenching from the melt (or melt spinning) [7]. Here, we illustrate several examples from our
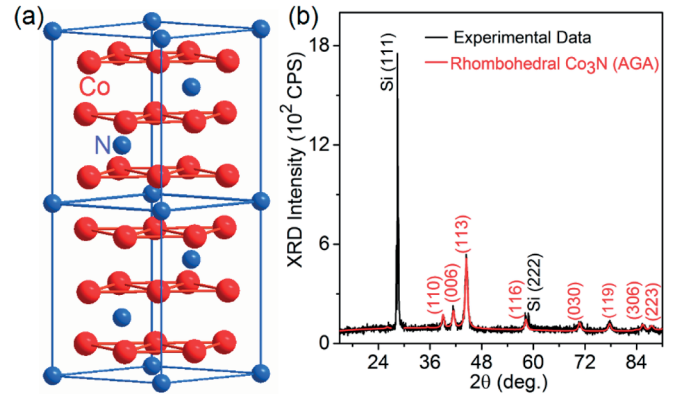

FIG. 11. (a) Schematic of a rhombohedral crystal structure of a Co$_3$N compound predicted by the AGA search [31]. (b) The experimental x-ray diffraction (XRD) pattern of the cluster-deposited Co$_3$N nanoparticles on a Si (111) substrate (black curve) is fit with the predicted rhombohedral structure using Rietveld analysis (red curve) [32].

synergistic computational and experimental efforts to discover new rare-earth-free magnetic materials.

A. Screening methods and its application

Our search process consists of three steps. In the first step, we use our AGA methods to explore structures across a wide range of chemical compositions. We predict numerous new stable and metastable intermetallic compounds enriched with Fe and/or Co as possible phases. In the second step, the electronic-structure calculations are performed to evaluate their intrinsic magnetic properties, with focus on finding materials that have the potential to exhibit high J_s, large K_1 (the MAE constant in the lowest order), and high T_c. In the third step, the screened materials with predicted compositions are fabricated using nonequilibrium fabrication methods and subsequently characterized using various structural and magnetic measurements. Our computational screening process helps to accelerate the optimization process during experiments, making it possible to avoid unnecessary experimental steps and reduce the combined search cost.

This scheme has been applied to a cobalt-nitride system [31]. Several metastable Co-N compounds are predicted using the AGA. Their intrinsic magnetic properties are estimated using DFT calculations. Figure 11(a) shows the schematic of a rhombohedral crystal structure of a Co$_3$N compound predicted by the AGA search. The DFT calculations yield $K_1 = 1.39$ MJ/m^3, $J_s = 0.83$ T, and $T_c = 336$ K for this structure.

These theoretical findings have assisted the synthesis of a set of new Co$_3$N compounds with desired magnetic properties in the form of nanoparticles using the cluster deposition method [32]. The cluster deposition method enables us to deposit a single phase of rhombohedral Co$_3$N in the form of nanoparticles on Si (111) substrates. As shown in Fig. 11(b), the experimental x-ray diffraction pattern for the nanoparticles shows the diffraction peaks corresponding to the Co$_3$N phase and additional peaks from the substrate. Excellent agreement exists between the experimental x-ray spectrum and the simulated spectrum using a Rietveld refinement analysis

based on the rhombohedral structure. The experimental lattice parameters, $a = 4.61$ Å and $c = 13.06$ Å, match with the theoretically predicted values, $a = 4.53$ Å and $c = 13.06$ Å. With magnetic measurements, we find $K_1 = 1.04$ MJ/m^3, $J_s = 0.73$ T, and $T_c \sim 450$ K for the rhombohedral Co$_3$N [32]. These numbers agree reasonably with the values predicted from first-principles calculations [31].

In our theoretical search, the AGA method enables us to explore a broad range of the compositional and structural space very efficiently. AGA searches yield dozens of stable and metastable structures, which we register as new candidate structures in our database. Our experimental search using nonequilibrium synthesis methods is confined to the compounds that can exhibit high J_s, large K_1, and high T_c. and often produced several compounds with high magnetic anisotropy predicted by the theoretical calculations. Still, the experimental synthesis of a desired compound is challenging in some cases. Our database has entries of not only the lowest formation-energy compounds (that are very likely to exist) but also several other compounds with the same or nearby stoichiometry that have the formation energies comparable to those of the most likely candidates.

In our AGA search and first-principles calculations, we find two Co$_3$N compounds with high magnetic anisotropy. The one crystallizes in the rhombohedral structure (space group of $R\bar{3}c$, lattice constants of $a = 4.53$ and $c = 13.06$ Å, and the formation energy above the hull of $+71.0$ meV/atom), and the other one in the orthorhombic structure (space group of *cmcm*, lattice constants of $a = 3.70$, $b = 11.29$, and $c = 3.77$ Å, and the formation energy above the hull of $+116.5$ meV/atom) [32]. Note that the above-mentioned formation energies of the Co$_3$N structures are calculated using hcp Co and N$_2$ as references and by following the equation,

$$\Delta E(\text{Co}_3\text{N}) = [E(\text{Co}_3\text{N}) - 0.5E(\text{N}_2) - 3E(\text{Co})]/4. \quad (6)$$

In this situation, our experimental synthesis only yielded the rhombohedral structure as schematically shown in Fig. 11(a), which has a lower formation energy above the hull.

Similarly, we carry out AGA searches for compounds with a nearby stoichiometry and discover two promising Co$_4$N phases that crystallize in a tetragonal structure with high K_1, J_s, and T_c [31]. The formation energies above the hull of the two Co$_4$N phases are comparable to but higher than that of the rhombohedral Co$_3$N structure. In this case, our experimental attempts to synthesize the Co$_4$N compounds only led to a mixture of Co plus Co$_4$N phases or Co$_3$N plus Co$_4$N phases.

B. AGA-assisted crystal structure determination

In experiment, various types of magnetic compounds have been synthesized so far. Some of them possess complex structure. For such compounds, it remains a challenging and time consuming task to determine the crystal structure and atomic arrangements (Wyckoff positions) using the experimental diffraction patterns. Precise atomic positions are essential to understand the magnetism in new compounds, especially for calculating their intrinsic magnetic properties.

A typical example is the intermetallic compound Zr$_2$Co$_{11}$, which has been fabricated in various ways [30,77–80]. Figure 12(a) shows a high-resolution transmission electron
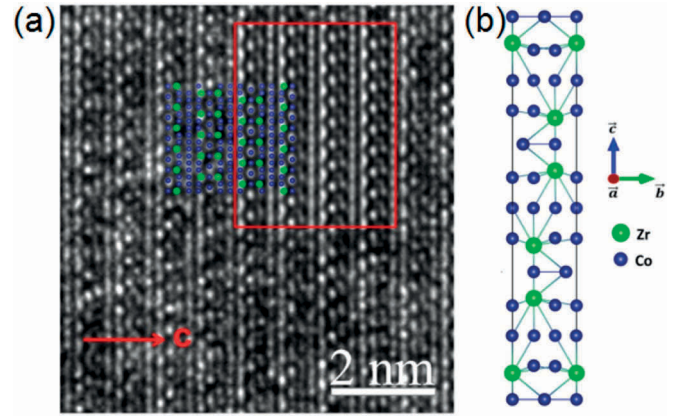

FIG. 12. (a) A high-resolution transmission electron microscope (HRTEM) image of the Zr$_2$Co$_{11}$ compound measured along the [010] zone axis. The red arrow indicates the repeated distance along the c axis. (b) Atomic structure for the rhombohedral Zr$_2$Co$_{11}$ phase solved by the AGA search. Inset within the red box in (a) is the simulated HREM image based on the structural model, and the structure model along the c axis is also laid on top of the experimental HRTEM image [28].

microscope (HRTEM) image of melt-spun Zr$_2$Co$_{11}$ [28]. Although 2:11 stoichiometry has been determined, it has been difficult to identify the crystal structure of Zr$_2$Co$_{11}$ using available experimental x-ray and electron diffraction patterns. Several complex crystal structures, including orthorhombic, rhombohedral, and hexagonal polymorphs, have been predicted to form near the Zr$_2$Co$_{11}$ stoichiometry [77–80].

Our AGA search is an efficient method to determine the crystal structure of a new compound. The structural determination is based solely on chemical composition. It does not require any assumptions on the Bravais lattice, atom basis, or unit-cell dimensions.

Recently, the AGA search solved the atomic structure of the rhombohedral Zr$_2$Co$_{11}$ phase [28]. Its space group is found to be $R32$ (space group No. 155). Its lattice constants are predicted to be $a = 4.69$ Å and $c = 24.0$ Å. The predicted lattice parameter c agrees well with the repeated distance along the c axis (~ 24.2 Å) measured from the HRTEM image of a melt-spun Zr$_2$Co$_{11}$ sample, shown in Fig. 12(a). In the red box of Fig. 12(a), we draw the structural projection and simulated atomic arrangements corresponding to the predicted rhombohedral phase [Fig. 12(b)]. The simulated structural model explains well the measured HRTEM image.

DFT calculations are carried out for Zr$_2$Co$_{11}$ in the predicted $R32$ structure, yielding the magnetic properties of $K_1 = 14.2$ Mergs/cm^3, $J_s = 10.1$ kG, and $T_c = 709$ K. These are in good agreement with the measured values ($K_1 = 13.5$ Mergs/cm^3, $J_s = 9.7$ kG, and $T_c = 783$ K) [30]. We confirm the consistency between the experimental observations and the theoretical findings. Our joint efforts on Zr$_2$Co$_{11}$ demonstrate the efficacy of our combined approach.

C. New magnets with high magnetic anisotropy

Our combined efforts have uncovered a series of novel Fe-, Co-, and Mn-rich magnetic compounds that are alloyed with magnetic or nonmagnetic element X ($X =$ N, Si, Sn,
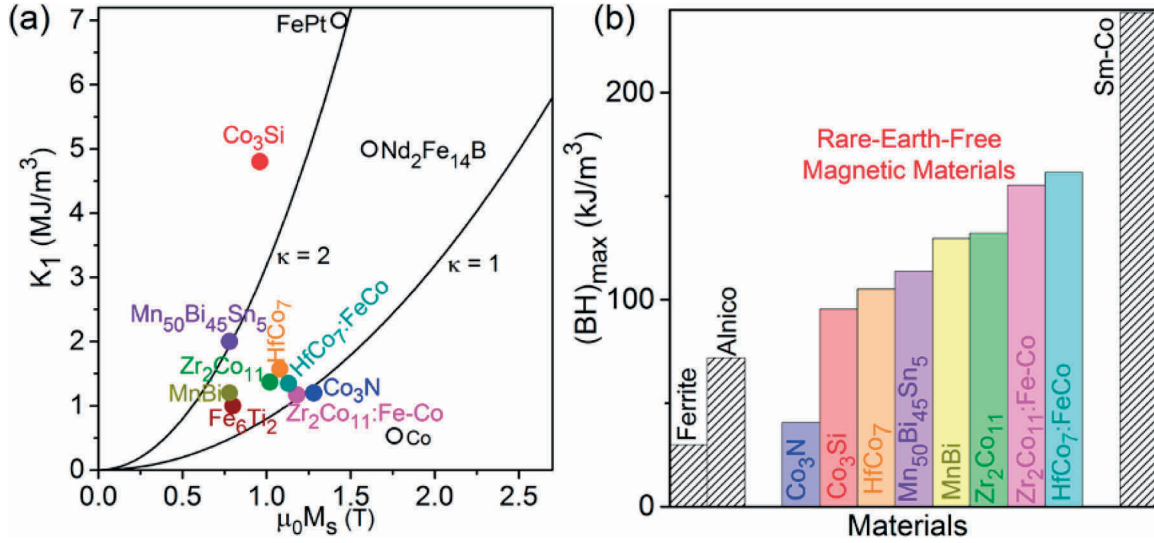
FIG. 13. Room-temperature magnetic properties of rare-earth-free magnetic materials. (a) Magnetocrystalline anisotropy constant K_1 versus saturation magnetic polarization $J_s = \mu_0 M_s$ (solid circles). Values of K_1 and J_s for Co, $Nd_2Fe_{14}B$, and $L1_0$-FePt are included for comparison (open circles). The parabolic curves correspond to the magnetic hardness parameters, $\kappa = 1$ and 2 are also shown. (b) Energy products of the rare-earth-free nanostructured magnetic materials are compared with those of traditional bulk magnets (gray-patterned bar graphs).

Zr, Hf, Y, C, S, Ti, or Bi). In these efforts, our main focus is on noncubic crystal structures to induce high magnetic anisotropy. Notable materials include (i) hexagonal structures of $Fe_3Co_3Ti_2$, $Fe_3Co_3Nb_2$, $Fe_{3+x}Co_{3-x}Ti_2$ ($0 \leqslant x \leqslant 3$), Co_3N, and Co_3Si, (ii) rhombohedral structures of Co_3N and Zr_2Co_{11}, (iii) a tetragonal structure of $Fe_8Co_8N_2$, and (iv) orthorhombic structures of $HfCo_7$ and Fe_2CoC [7]. These compounds are free from critical rare-earth elements and expensive Pt. Most of them exhibit appreciable magnetic anisotropy ($K_1 \geqslant 1$ MJ/m^3), large magnetization ($J_s \geqslant 1$ T), and high Curie temperature ($T_c \geqslant 300$ K).

The magnetocrystalline anisotropy is a key intrinsic property of a magnet. It plays an important role in permanent magnets and data storage. In particular, a large K_1 is desirable to develop high coercivity. The coercivity H_c is ideally equivalent to the anisotropy field H_a and is inversely proportional to M_s, namely,

$$H_c = H_a = 2K_1/M_s. \qquad (7)$$

A permanent-magnet material should have not only a large M_s but also a sufficiently large H_a to exhibit high H_c. As mentioned in Sec. V B, magnetic materials with $\kappa \geqslant 1$ are promising for permanent-magnet applications. Most of the Fe-, Co-, and Mn-rich compounds found by our experimental search fall in this category, as shown in Fig. 13(a).

The energy product $(BH)_{\max}$ is a key figure of merit in permanent magnets. It is defined as the maximum of the product of B and H in the second quadrant of the B-H curve, where $B = \mu_0(H + M)$ is the flux density or magnetic-field induction. The maximum theoretical energy product achievable for a magnetic material is

$$(BH)_{\max}^{\text{th}} = J_s^2/4. \qquad (8)$$

Figure 13(a) shows that our new compounds have J_s of 0.75–1.25 T. These materials have the potential to exhibit room-temperature energy products of 111–318 kJ/m^3

(equivalent to 14–40 MGOe), which are higher than those of the traditional rare-earth-free magnets, such as ferrites ($\sim$30 kJ/m^3) and "alnico ($\sim$72 kJ/m^3)," a family of alloys made of iron, aluminium, nickel, and cobalt. Moreover, these values are comparable to those of rare-earth-based Sm-Co alloys ($\sim$239 kJ/m^3). Practically, maximum room-temperature energy products of 41–162 kJ/m^3 are achieved in the nanostructured films of the new rare-earth-free materials [32,81–85], as shown in Fig. 13(b). If appropriate scale-up methods for bulk production of these new compounds are developed, these materials can be used for applications, where cost-effective magnets with the intermediate performance between alnico and rare-earth-based magnets are highly expected [74].

D. New magnets for data-storage applications

High uniaxial anisotropy is essential to improve the thermal stability of written bits (grains) in high-density recording media [8,9]. The MAE constant for uniaxial anisotropy, K_u, can be expanded in terms of spherical polar coordinates. The MAE constant of the lowest order, which is given by Eq. (1), is a leading term of K_u. The potential of a magnetic material as recording media can be assessed by using the stability criterion ξ, written as

$$\xi = K_u V/k_B T \geqslant 50, \qquad (9)$$

where V and k_B are the volume of the grains and the Boltzmann constant, respectively. The areal density can be deduced from the thermally stable minimal grain size D_p of a magnetic material. In a perpendicular recording media, the grain size can be written as

$$D_p = \left[\frac{2k\xi k_B T}{H_a M_s (1 - 4\pi M_s/H_a)^2} \right]^n, \qquad (10)$$

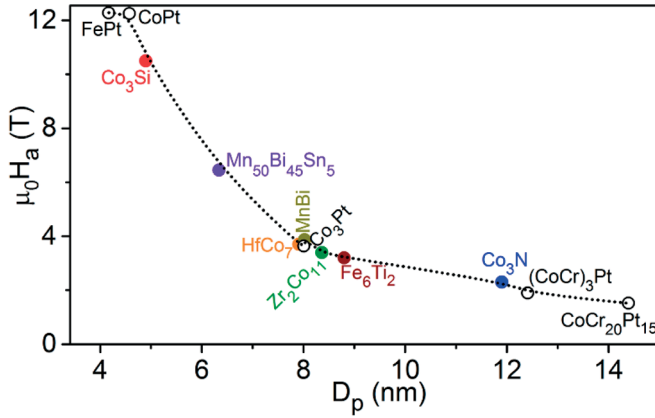where $k = 6/\pi$ and $n = 1/3$ for spherical grains [9].

FIG. 14. Magnetic anisotropy field $\mu_0 H_a$ versus estimated minimal stable spherical grain diameter D_p at room temperature for the rare-earth- and Pt-free magnetic materials (solid circles). Those values for some of the traditional Pt-based alloys are also given for comparison (open circles).

In order to explore the prospect of new magnetic compounds, we evaluate the spherical grain size D_p at room temperature using $\xi = 50$. Figure 14 shows the magnetic anisotropy field $\mu_0 H_a$ as a function of the estimated D_p values. The estimated D_p values of our new compounds are comparable with those of Pt-based materials. Note that the D_p values of our Pt-free compounds can be further decreased if these materials are fabricated in the form of cylindrical grains or elongated cubes. Significant research efforts have to be initiated, with the help of the combined screening methods, towards the discovery of new cost-effective materials for practical data-storage applications.

VII. PERSPECTIVE

The number of known structures of binary, ternary, and quaternary compounds available for making magnets is much less than that of possible structures and compounds. There is great possibility for the discovery of new magnetic materials. Yet, it is a difficult task to predict a new structure that is viable *and* has desired magnetic properties. There are numerous candidate compounds owing to a myriad of possible combinations of available elements across the periodic table. Even for a particular chemical composition (stoichiometry), several polymorphs can exist.

The use of artificial intelligence (AI) methods, such as machine-learning algorithms and neural network models, is setting the trend for the design of new advanced materials [10,11]. The basic idea behind the AI-based approach is to make an instant assessment of materials properties in the hope of speeding up a whole search process. For example, researchers develop machine-learning models to find the relationship between material and its Curie temperature [86,87]. AI-based computational screening may offer a tool to seek out promising structures from a large number of candidate structures.

In traditional computational approaches, it is essential to solve the basic equations to understand ("deduce") material properties from first principles. In contrast, AI-assisted material discovery is a data-driven *inductive* approach. Sample data, called training data, is used as input for building a predictive AI model. Such training data can be a collection of representative data from experiments and calculations. In a machine-learning approach, learning on database space is a very important step to help close the gap between known and predicted properties.

Basic material properties can be extracted from several open-access databases [12–17]. However, these database provide little information about the magnetic properties. In particular, a serious drawback is the sparsity of the microscopic magnetic properties. Our database provides both macroscopic ("lattice-wide") and microscopic ("site-resolved") magnetic data for crystalline magnetic materials. Our database also provides magnetic properties of transition-metal-based nanoclusters on an equal footing. Such a dataset is scarce in other databases to date. There is a great advantage to using our detailed data as training data for AI-based design of rare-earth-free magnetic materials.

Our database contains many stable and metastable compounds discovered from our AGA searches. Our AGA structures are enriched with Fe and Co. They are free from rare earths and expensive metals. As illustrated in Sec. VI, our AGA-based screening scheme assisted the experimental discoveries of new rare-earth-free magnetic materials. Subsequent experimental characterization confirmed the potential of new magnetic materials as permanent magnets and recording media. These results indicate that our combined search techniques can be applied to a broader class of magnetic materials. The combination of our extensive datasets and advanced data-mining techniques makes it possible to better identify synthesizable candidate magnets that are free from critical and expensive elements.

Our database will be expanded by employing the AGA method to possible combinations of two or more elements, with focus on Fe-based and Co-based systems doped with $2p$ and $3p$ elements or $3d$ metals. Computational efforts with AGA will bring many possible compounds that can hardly be found in other databases. Increasing of the number of data points in compositional and structural space will reinforce the efficiency of computational screening. Subsequent high-throughput first-principles calculations will make it possible to assess the stability of new structures, update the phase diagram, and possibly revise the convex hull (the compositional dependence of the lower limit in the formation energy). Increasing the amount of data for site-resolved magnetic properties will also be highly beneficial to materials design using data-mining techniques. A feedback loop of predictions and experiments will certainly accelerate the experimental discovery of new magnetic materials, as illustrated in the previous section.

VIII. SUMMARY

We developed an open-access database specialized for magnetic materials. Our database possesses a number of unique features: (i) new stable and metastable structures discovered through our AGA searches, (ii) the site-specific magnetic data from high-throughput first-principles calculations, (iii) massive datasets for crystals and clusters, and (iv) the automated web applications in close cooperation with the online database. We illustrated that our data-intensive meth-

ods improve efficiency of the experimental fabrication of new rare-earth-free and Pt-free magnetic materials. The fabricated materials show promising magnetic properties for permanent-magnet and data-storage applications. Our database provides a solid platform that guides the theoretical and experimental design of new rare-earth-free magnetic materials, especially when coupled with AI methods.

[1] J. M. D. Coey and H. Sun, Improved magnetic properties by treatment of iron-based rare earth intermetallic compounds in anmonia, J. Magn. Magn. Mater. **87**, L251 (1990).

[2] J. F. Herbst, $R_2Fe_{14}B$ materials: Intrinsic properties and technological aspects, Rev. Mod. Phys. **63**, 819 (1991).

[3] J. M. D. Coey, Permanent magnets: Plugging the gap, Scr. Mater. **67**, 524 (2012).

[4] T. Miyake, K. Terakura, Y. Harashima, H. Kino, and S. Ishibashi, First-principles study of magnetocrystalline anisotropy and magnetization in $NdFe_{12}$, $NdFe_{11}Ti$, and $NdFe_{11}TiN$, J. Phys. Soc. Jpn. **83**, 043702 (2014).

[5] T. Miyake and H. Akai, Quantum theory of rare-earth magnets, J. Phys. Soc. Jpn. **87**, 041009 (2018).

[6] J. Cui, M. Kramer, L. Zhou, F. Liu, A. Gabay, G. Hadjipanayis, B. Balasubramanian, and D. Sellmyer, Current progress and future challenges in rare-earth-free permanent magnets, Acta Mater. **158**, 118 (2018).

[7] B. Balasubramanian, M. Sakurai, C.-Z. Wang, X. Xu, K.-M. Ho, J. R. Chelikowsky, and D. J. Sellmyer, Synergistic computational and experimental discovery of novel magnetic materials, Mol. Syst. Des. Eng. **5**, 1098 (2020).

[8] C. Tannous and R. L. Comstock, Magnetic information-storage materials, in *Springer Handbook of Electronic and Photonic Materials*, edited by S. Kasap and P. Capper (Springer International Publishing, Cham, 2017), pp. 1185–1223.

[9] D. Weller and T. McDaniel, Media for extremely high density recording, in *Advanced Magnetic Nanostructures*, edited by D. Sellmyer and R. Skomski (Springer US, Boston, 2006), pp. 295–324.

[10] K. T. Butler, D. W. Davies, H. Cartwright, O. Isayev, and A. Walsh, Machine learning for molecular and materials science, Nature (London) **559**, 547 (2018).

[11] J. E. Gubernatis and T. Lookman, Machine learning in materials design and discovery: Examples from the present and suggestions for the future, Phys. Rev. Materials **2**, 120301 (2018).

[12] S. Curtarolo, W. Setyawan, G. L. Hart, M. Jahnatek, R. V. Chepulskii, R. H. Taylor, S. Wang, J. Xue, K. Yang, O. Levy, M. J. Mehl, H. T. Stokes, D. O. Demchenko, and D. Morgan, AFLOW: An automatic framework for high-throughput materials discovery, Comput. Mater. Sci. **58**, 218 (2012).

[13] http://aflowlib.org.

[14] A. Jain, S. P. Ong, G. Hautier, W. Chen, W. D. Richards, S. Dacek, S. Cholia, D. Gunter, D. Skinner, G. Ceder, and K. A. Persson, Commentary: The materials project: A materials genome approach to accelerating materials innovation, APL Mater. **1**, 011002 (2013).

[15] https://materialsproject.org.

[16] J. E. Saal, S. Kirklin, M. Aykol, B. Meredig, and C. Wolverton, Materials design and discovery with high-throughput density functional theory: The open quantum materials database (OQMD), JOM **65**, 1501 (2013).

[17] http://oqmd.org.

[18] https://repository.nomad-coe.eu.

[19] S. Sanvito, C. Oses, J. Xue, A. Tiwari, M. Zic, T. Archer, P. Tozman, M. Venkatesan, M. Coey, and S. Curtarolo, Accelerated discovery of new magnets in the heusler alloy family, Sci. Adv. **3**, e1602241 (2017).

[20] http://webbdcrista1.ehu.es/magndata/.

[21] P. Nieves, S. Arapan, J. Maudes-Raedo, R. Marticorena-Sánchez, N. Del Brío, A. Kovacs, C. Echevarria-Bonet, D. Salazar, J. Weischenberg, H. Zhang, O. Vekilova, R. Serrano-López, J. Barandiaran, K. Skokov, O. Gutfleisch, O. Eriksson, H. Herper, T. Schrefl, and S. Cuesta-López, Database of novel magnetic materials for high-performance permanent magnet development, Comput. Mater. Sci. **168**, 188 (2019).

[22] http://crono.ubu.es/novamag.

[23] Visit our portal page at https://www.novomag.physics.iastate.edu/structure-database that will navigate to our Magnetic Materials Database and web applications.

[24] D. M. Deaven and K. M. Ho, Molecular Geometry Optimization With A Genetic Algorithm, Phys. Rev. Lett. **75**, 288 (1995).

[25] S. Q. Wu, M. Ji, C. Z. Wang, M. C. Nguyen, X. Zhao, K. Umemoto, R. M. Wentzcovitch, and K. M. Ho, An adaptive genetic algorithm for crystal structure prediction, J. Phys.: Condens. Matter **26**, 035402 (2013).

[26] P. Brommer and F. Gähler, Potfit: effective potentials from *ab initio* data, Model. Simul. Mater. Sci. Eng. **15**, 295 (2007).

[27] X. Zhao, S. Q. Wu, M. C. Nguyen, K.-M. Ho, and C.-Z. Wang, Adaptive genetic algorithm for structure prediction and application to magnetic materials, in *Handbook of Materials Modeling*, Vol. 2, edited by W. Andreoni and S. Yip, 2nd ed. (Springer International Publishing, Switzerland, 2019).

[28] X. Zhao, M. C. Nguyen, W. Y. Zhang, C. Z. Wang, M. J. Kramer, D. J. Sellmyer, X. Z. Li, F. Zhang, L. Q. Ke, V. P. Antropov, and K. M. Ho, Exploring The Structural Complexity Of Intermetallic Compounds By An Adaptive Genetic Algorithm, Phys. Rev. Lett. **112**, 045502 (2014).

[29] X. Zhao, C.-Z. Wang, Y. Yao, and K.-M. Ho, Large magnetic anisotropy predicted for rare-earth-free $Fe_{16-x}Co_xN_2$ alloys, Phys. Rev. B **94**, 224424 (2016).

[30] B. Balamurugan, B. Das, W. Y. Zhang, R. Skomski, and D. J. Sellmyer, Hf–Co and Zr–Co alloys for rare-earth-free permanent magnets, J. Phys.: Condens. Matter **26**, 064204 (2014).

[31] X. Zhao, L. Ke, C.-Z. Wang, and K.-M. Ho, Metastable cobalt nitride structures with high magnetic anisotropy for rare-earth free magnets, Phys. Chem. Chem. Phys. **18**, 31680 (2016).

[32] B. Balasubramanian, X. Zhao, S. R. Valloppilly, S. Beniwal, R. Skomski, A. Sarella, Y. Jin, X. Li, X. Xu, H. Cao, H. Wang, A. Enders, C.-Z. Wang, K.-M. Ho, and D. J. Sellmyer, Magnetism of new metastable cobalt-nitride compounds, Nanoscale **10**, 13011 (2018).

[33] V. Gvozdetskyi, G. Bhaskar, M. Batuk, X. Zhao, R. Wang, S. L. Carnahan, M. P. Hanrahan, R. A. Ribeiro, P. C. Canfield, A. J. Rossini, C.-Z. Wang, K.-M. Ho, J. Hadermann, and J. V. Zaikina, Computationally driven discovery of a family of layered LiNiB polymorphs, Angew. Chem. Int. Ed. **58**, 15855 (2019).

[34] R. Wang, Y. Sun, V. Gvozdetskyi, X. Zhao, F. Zhang, L.-H. Xu, J. V. Zaikina, Z. Lin, C.-Z. Wang, and K.-M. Ho, Theoretical search for possible Li-Ni-B crystal structures using an adaptive genetic algorithm, J. Appl. Phys. **127**, 094902 (2020).

[35] P. Hohenberg and W. Kohn, Inhomogeneous electron gas, Phys. Rev. **136**, B864 (1964).

[36] W. Kohn and L. J. Sham, Self-consistent equations including exchange and correlation effects, Phys. Rev. **140**, A1133 (1965).

[37] P. E. Blöchl, Projector augmented-wave method, Phys. Rev. B **50**, 17953 (1994).

[38] J. P. Perdew, K. Burke, and M. Ernzerhof, Generalized Gradient Approximation Made Simple, Phys. Rev. Lett. **77**, 3865 (1996).

[39] H. J. Monkhorst and J. D. Pack, Special points for brillouin-zone integrations, Phys. Rev. B **13**, 5188 (1976).

[40] G. Kresse and J. Furthmüller, Efficiency of ab-initio total energy calculations for metals and semiconductors using a plane-wave basis set, Comput. Mater. Sci. **6**, 15 (1996).

[41] G. Kresse and J. Furthmüller, Efficient iterative schemes for ab initio total-energy calculations using a plane-wave basis set, Phys. Rev. B **54**, 11169 (1996).

[42] P. Giannozzi, S. Baroni, N. Bonini, M. Calandra, R. Car, C. Cavazzoni, D. Ceresoli, G. L. Chiarotti, M. Cococcioni, I. Dabo, A. D. Corso, S. de Gironcoli, S. Fabris, G. Fratesi, R. Gebauer, U. Gerstmann, C. Gougoussis, A. Kokalj, M. Lazzeri, L. Martin-Samos, N. Marzari, F. Mauri, R. Mazzarello, S. Paolini, A. Pasquarello, L. Paulatto, C. Sbraccia, S. Scandolo, G. Sclauzero, A. P. Seitsonen, A. Smogunov, P. Umari, and R. M. Wentzcovitch, QUANTUM ESPRESSO: a modular and open-source software project for quantum simulations of materials, J. Phys.: Condens. Matter **21**, 395502 (2009).

[43] A. Liechtenstein, M. Katsnelson, V. Antropov, and V. Gubanov, Local spin density functional approach to the theory of exchange interactions in ferromagnetic metals and alloys, J. Magn. Magn. Mater. **67**, 65 (1987).

[44] O. K. Andersen, Linear methods in band theory, Phys. Rev. B **12**, 3060 (1975).

[45] M. van Schilfgaarde and V. P. Antropov, First-principles exchange interactions in Fe, Ni, and Co, J. Appl. Phys. **85**, 4827 (1999).

[46] V. P. Antropov, B. N. Harmon, and A. N. Smirnov, Aspects of spin dynamics and magnetic interactions, J. Magn. Magn. Mat. **200**, 148 (1999).

[47] D. Pashov, S. Acharya, W. R. Lambrecht, J. Jackson, K. D. Belashchenko, A. Chantis, F. Jamet, and M. van Schilfgaarde, Questaal: A package of electronic structure methods based on the linear muffin-tin orbital technique, Comput. Phys. Commun. **249**, 107065 (2020).

[48] M. Sakurai, X. Zhao, C.-Z. Wang, K.-M. Ho, and J. R. Chelikowsky, Influence of nitrogen dopants on the magnetization of Co_3N clusters, Phys. Rev. Materials **2**, 024401 (2018).

[49] M. L. Tiago, Y. Zhou, M. M. G. Alemany, Y. Saad, and J. R. Chelikowsky, Evolution Of Magnetism In Iron From The Atom To The Bulk, Phys. Rev. Lett. **97**, 147201 (2006).

[50] J. Souto-Casares, M. Sakurai, and J. R. Chelikowsky, Structural and magnetic properties of large cobalt clusters, Phys. Rev. B **93**, 174418 (2016).

[51] M. Sakurai, J. Souto-Casares, and J. R. Chelikowsky, Size dependence of structural stability and magnetization of nickel clusters from real-space pseudopotentials, Phys. Rev. B **94**, 024437 (2016).

[52] R. H. Byrd, P. Lu, J. Nocedal, and C. Zhu, A limited memory algorithm for bound constrained optimization, SIAM J. Sci. Comput. **16**, 1190 (1995).

[53] C. Zhu, R. H. Byrd, P. Lu, and J. Nocedal, Algorithm 778: L-BFGS-B: Fortran subroutines for large-scale bound-constrained optimization, ACM Trans. Math. Software **23**, 550 (1997).

[54] J. L. Morales and J. Nocedal, Remark on "algorithm 778: L-BFGS-B: Fortran subroutines for large-scale bound constrained optimization," ACM Trans. Math. Software **38**, 1 (2011).

[55] J. R. Chelikowsky, N. Troullier, and Y. Saad, Finite-Difference-Pseudopotential Method: Electronic Structure Calculations Without A Basis, Phys. Rev. Lett. **72**, 1240 (1994).

[56] J. R. Chelikowsky, N. Troullier, K. Wu, and Y. Saad, Higher-order finite-difference pseudopotential method: An application to diatomic molecules, Phys. Rev. B **50**, 11355 (1994).

[57] L. Kronik, A. Makmal, M. L. Tiago, M. M. G. Alemany, M. Jain, X. Huang, Y. Saad, and J. R. Chelikowsky, PARSEC - the pseudopotential algorithm for real-space electronic structure calculations: recent advances and novel applications to nanostructures, Phys. Status Solidi B **243**, 1063 (2006).

[58] M. Sakurai and J. R. Chelikowsky, Enhanced magnetic moments in Mn-doped FeCo clusters owing to ferromagnetic surface Mn atoms, Phys. Rev. Materials **3**, 044402 (2019).

[59] Y. Zhou, Y. Saad, M. L. Tiago, and J. R. Chelikowsky, Parallel self-consistent-field calculations via Chebyshev-filtered subspace acceleration, Phys. Rev. E **74**, 066704 (2006).

[60] Y. Zhou, Y. Saad, M. L. Tiago, and J. R. Chelikowsky, Self-consistent-field calculations using Chebyshev-filtered subspace iteration, J. Comput. Phys. **219**, 172 (2006).

[61] Y. Zhou, J. R. Chelikowsky, and Y. Saad, Chebyshev-filtered subspace iteration method free of sparse diagonalization for solving the Kohn-Sham equation, J. Comput. Phys. **274**, 770 (2014).

[62] https://www.iucr.org/resources/cif.

[63] https://yaml.org.

[64] https://www.python.org.

[65] https://pymatgen.org.

[66] https://www.mongodb.com.

[67] https://palletsprojects.com/p/flask.

[68] https://palletsprojects.com/p/jinja.

[69] https://www.heroku.com.

[70] https://matplotlib.org.

[71] https://www.iucr.org.

[72] https://lammps.sandia.gov.

[73] https://www.json.org.

[74] R. Skomski and J. M. D. Coey, Magnetic anisotropy – how much is enough for a permanent magnet? Scripta Mater. **112**, 3 (2016).

[75] G. H. O. Daalderop, P. J. Kelly, and M. F. H. Schuurmans, Magnetocrystalline anisotropy of YCo_5 and related $RECo_5$ compounds, Phys. Rev. B **53**, 14415 (1996).

[76] V. Antropov, L. Ke, and D. Åberg, Constituents of magnetic anisotropy and a screening of spin-orbit coupling in solids, Solid State Commun. **194**, 35 (2014)

[77] B. G. Demczyk and S. F. Cheng, Structures of Zr_2Co_{11} and $HfCo_7$ intermetallic compounds, J. Appl. Cryst. **24**, 1023 (1991).

[78] A. Gabay, Y. Zhang, and G. Hadjipanayis, Cobalt-rich magnetic phases in Zr-Co alloys, J. Magn. Magn. Mater. **236**, 37 (2001).

[79] G. Ivanova, N. Shchegoleva, and A. Gabay, Crystal structure of Zr_2Co_{11} hard magnetic compound, J. Alloys Compd. **432**, 135 (2007).

[80] G. Ivanova and N. Shchegoleva, The microstructure of a magnetically hard Zr_2Co_{11} alloy, Phys. Metals Metallogr. **107**, 270 (2009).

[81] B. Balasubramanian, P. Manchanda, R. Skomski, P. Mukherjee, S. R. Valloppilly, B. Das, G. C. Hadjipanayis, and D. J. Sellmyer, High-coercivity magnetism in nanostructures with strong easy-plane anisotropy, Appl. Phys. Lett. **108**, 152406 (2016).

[82] W. Zhang, B. Balasubramanian, P. Kharel, R. Pahari, S. R. Valloppilly, X. Li, L. Yue, R. Skomski, and D. J. Sellmyer, High energy product of MnBi by field annealing and Sn alloying, APL Mater. **7**, 121111 (2019).

[83] B. Balasubramanian, B. Das, R. Skomski, W. Y. Zhang, and D. J. Sellmyer, Magnetic materials: Novel nanostructured rare-earth-free magnetic materials with high energy products (adv. mater. 42/2013), Adv. Mater. **25**, 6089 (2013).

[84] B. Balasubramanian, P. Mukherjee, R. Skomski, P. Manchanda, B. Das, and D. J. Sellmyer, Magnetic nanostructuring and overcoming brown's paradox to realize extraordinary high-temperature energy products, Sci. Rep. **4**, 6265 (2014).

[85] W. Zhang, P. Kharel, S. Valloppilly, L. Yue, and D. J. Sellmyer, High-energy-product MnBi films with controllable anisotropy, Phys. Status Solidi B **252**, 1934 (2015).

[86] H. C. Dam, V. C. Nguyen, T. L. Pham, A. T. Nguyen, K. Terakura, T. Miyake, and H. Kino, Important descriptors and descriptor groups of curie temperatures of rare-earth transition-metal binary alloys, J. Phys. Soc. Jpn. **87**, 113801 (2018).

[87] J. Nelson and S. Sanvito, Predicting the curie temperature of ferromagnets using machine learning, Phys. Rev. Materials **3**, 104405 (2019).